Nanoscale Advances

ROYAL SOCIETY OF CHEMISTRY

PAPER

View Article Online
View Journal | View Issue

Cite this: *Nanoscale Adv.*, 2025, **7**, 1851

Highly efficient catalytic hydrogenation of *p*-chloronitrobenzene: the synergistic effect and hybrid nano-structure†

Yanji Zhang *[a] and Jicheng Zhou[b]

Noble metal catalysts have attracted worldwide attention for catalytic selective hydrogenation due to their high activity. However, constructing highly effective, selective, and stable noble metal catalysts remains challenging. Herein, zirconium/zeolite supported platinum catalysts have been prepared. These hybrid nano-structured Pt/ZrO_2/ZSM-5 and Pt/ZrO_2/MCM-22 catalysts (denoted as Pt/ZZ and Pt/ZM) exhibited superior catalytic performance for the selective hydrogenation of *p*-chloronitrobenzene (*p*-CNB), which was much higher than that of Pt/ZrO_2, Pt/ZSM-5, and Pt/MCM-22, demonstrating the synergistic effect in these hybrid nano-structured catalysts. Especially, the turnover frequency (TOF) of Pt/ZM was as high as 8525 h^{-1}, surpassing that of most reported noble metal and novel non-noble metal catalysts, and the catalyst can be recycled for six runs without any obvious decrease in activity and selectivity. The characterization indicated that the electron transfer from Pt to ZrO_2 can greatly facilitate the performance of *p*-CNB hydrogenation through modulating the electronic structure and surface structure. This work provides an effective strategy for the design of noble metal catalysts with high activity and selectivity.

Received 20th October 2024
Accepted 17th January 2025

DOI: 10.1039/d4na00870g

rsc.li/nanoscale-advances

1 Introduction

Over the past few decades, noble metal catalysts have played an important role in selective hydrogenation due to their excellent performance.[1–4] Notably, side reactions were unavoidable on these single-metal-based catalysts, such as complete hydrogenation, competition from other reducible functional groups, or group breaking. Furthermore, agglomeration or leaching of metal nanoparticles often occurred, leading to poor selectivity and catalytic activity.[5–7] Therefore, the development of advanced catalysts that are stable, easy-to-handle, highly active, and selective has become a subject of urgent research, although this goal is challenging.

As we all know, both noble metals and supports play a crucial role because H_2 can be adsorbed and dissociated on a noble metal site, and the substrates hydrogenate on the support.[8] Noble metals, especially Pt[9–12] and Pd,[13–15] have been intensively used in fabricating heterogeneous catalysts because of their remarkable activity for hydrogen activation. Meanwhile, the downside is that when C–X (X = F, Cl, Br, and I) coexists with –NO_2, selective conversion of –NO_2 to –NH_2 will be accompanied by dehalogenation, affecting selectivity.[16] Therefore, it is very important and urgent to design and prepare highly efficient noble metal catalysts.

In fact, the supports not only stabilize the dispersed metals but also modify their morphology and electronic structure through interaction with them, the so-called metal–support interaction.[17] Taking advantage of this interaction to adjust the catalyst performance has been the most popular approach. Recently, some selective hydrogenation catalysts have been developed by choosing suitable supports, which enhance activity due to their architecture and interaction with noble metals. Various advanced materials have been reported because of significant improvements in synthetic methods and characterization techniques.

Zeolite, a unique inorganic crystalline aluminosilicate, with a high surface area, improves the dispersity of metals and provides reaction sites, contributing to the adsorption of substrate molecules. Thus, it has been widely used in selective hydrogenation.[1,18,19] Chen *et al.*[20] encapsulated Pt clusters into sodalite (SOD) zeolite, and the structure of SOD zeolite prevented the direct interaction between Pt and *p*-CNB, avoiding the simultaneous activation of the nitro group and C–Cl group on the encapsulated Pt surface. Instead, selective hydrogenation of nitro was achieved through the hydrogen overflow process. Zhang and Yin[21] reported a synthesis strategy for encapsulating Pd nanoclusters into zeolite using a high-temperature soft gel system. The prepared Pd@S-1-SGP catalyst exhibited higher selectivity for *p*-chloroaniline (*p*-CAN) compared to Pd/SiO_2 in the selective hydrogenation of *p*-CNB

[a]*School of Chemistry and Materials Engineering, Quzhou University, Quzhou 324000, Zhejiang Province, China. E-mail: zhangyanji2017@126.com*

[b]*Key Laboratory of Green Catalysis and Chemical Reaction Engineering of Hunan Province, School of Chemical Engineering, Xiangtan University, Xiangtan 411105, Hunan Province, China*

† Electronic supplementary information (ESI) available. See DOI: https://doi.org/10.1039/d4na00870g

due to the steric structure of zeolite micropores favoring selective adsorption of the nitro group over the C–Cl group on the Pd surface. Yang[22] fabricated a core–shell structured Pd@TS-1@meso-SiO_2 catalyst, and the acid sites and protection provided by the mesoporous silica shell enhanced its activity. As can be seen, the most important design concept of the above-reported catalysts is the encapsulation of noble metals within zeolites. On the one hand, the mesoporous shell prevents noble metal leaching and improves stability. On the other hand, molecules are adsorbed in a sterically controlled manner and selectively transformed within the zeolite pores, improving product selectivity.

It is known that the catalytic performance is highly dependent on the establishment of a structure–performance relationship, which can generate additional interface effects, such as strong metal–support interaction (SMSI), oxygen vacancies, or electronic effect.[23] Typically, noble metal nanoparticles are supported on metal oxide supports such as CeO_2,[24] TiO_2,[5,25] and Fe_2O_3.[8] Since 2006, Corma and coworkers[26–28] have reported the high chemoselectivity of Au/TiO_2 and Pt/TiO_2 catalysts, indicating that energetically and geometrically favored adsorption through the nitro group occurs on the TiO_2 support and at the interface between the nanoparticle and the TiO_2 support. In previous work,[29–33] we combined metal oxides (TiO_2, CeO_2, La_2O_3, and ZrO_2) and supports with a large specific surface area (activated carbon and SBA-15) to fabricate a series of hybrid nano-structured noble metal catalysts. Among these, the Pt/@-ZrO_2/SBA-15 catalyst exhibited remarkable catalytic activity in the selective hydrogenation of the C=O bond, $-NO_2$ groups, and C=C bond, and the TOF reached 4822 h^{-1}, 57 588 h^{-1}, and 66 790 h^{-1} in the selective hydrogenation of benzaldehyde, *p*-CNB, and styrene, respectively. According to in-depth research, we found that the strong interface electronic effect and the unique properties of the special hybrid nano-structure contribute significantly.

Herein, we report simple and highly efficient Pt/ZrO_2/ZSM-5 and Pt/ZrO_2/MCM-22 catalysts (denoted as Pt/ZZ and Pt/ZM), obtained by a photochemical route, which exhibit excellent activity, selectivity, and stability for the selective hydrogenation of *p*-CNB under mild conditions. By combining metal oxides with zeolite, the prepared catalysts not only take advantage of the properties of ZrO_2 but also retain the structures of ZSM-5 or MCM-22. It is not necessary to deliberately encapsulate the noble metal; instead, the catalysts can maintain stability and selectivity even at low noble metal loading (0.08% Pt). Furthermore, the special structure generates a synergistic effect, achieving a TOF of 5323 h^{-1} and 8525 h^{-1} for Pt/ZZ and Pt/ZM, respectively. This study provides a new approach for the design of supported metal catalysts that have great practical potential for selective hydrogenation of various nitroarenes.

2 Experimental

2.1 Materials

All chemicals were purchased from chemical companies and used without further purification: zirconium oxide chloride, ammonia monohydrate (Tianjin Ke Miou Chemical Reagent Co., Ltd), ZSM-5 or MCM-22 (the catalyst plant of Nankai University), H_2PtCl_6 (7.4 mg mL^{-1}), *p*-chloroaniline (Shanghai Maclean Biochemical Technology Co., Ltd), and ethanol (Tianjin Ke Miou Chemical Reagent Co., Ltd).

2.2 Preparation of catalysts

Typically, 0.291 g of $ZrOCl_2 \cdot 8H_2O$ and 10 mL of deionized water were added to a beaker and magnetically stirred until the solid was dissolved. Then, 1 g of MCM-22 or ZSM-5 was added to the above solution, and after thoroughly mixing, the pH was adjusted to 10 using 1.5 mol L^{-1} $NH_3 \cdot H_2O$, followed by aging for 24 h. Finally, the composite carrier ZrO_2/MCM-22 or ZrO_2/ZSM-5 was obtained by filtration and washing with deionized water several times, drying at 100 °C and calcining at 500 °C for 4 h. The preparation of ZrO_2 was the same as above, with the addition of MCM-22 or ZSM-5. 0.497 g ZrO_2/MCM-22 or ZrO_2/ZSM-5, 100 mL deionized water, 5 mL methanol, and 0.68 mL H_2PtCl_6 were mixed and stirred for 10 h under ultraviolet light. Subsequently, the solution was filtered and washed with deionized water several times and then dried in a vacuum oven at 80 °C, yielding the Pt/ZZ and Pt/ZM catalysts.

2.3 Catalytic hydrogenation reaction

0.05 g catalyst, 0.2 g *p*-CNB, and 20 mL ethanol were added into an autoclave (50 mL). The air was first replaced with 99.99% H_2 five times, and then the autoclave was filled with H_2 to 0.7 MPa. The temperature was raised to 40 °C, and the mixture was stirred at 800 rpm for 1.5 h. Finally, the reactor was moved to an ice-water bath to cool down. The reaction solution was obtained by filtration and analyzed using an Agilent 6890N GC with an HP-5 capillary column and FID detector.

$$\text{Conversion (\%)} = (n^0_{p\text{-CNB}} - n_{p\text{-CNB}})/n^0_{p\text{-CNB}} \times 100\%$$

$$\text{Selectivity (\%)} = n_{p\text{-CAN}}/(n^0_{p\text{-CNB}} - n_{p\text{-CNB}}) \times 100\%$$

$$\text{TOF} = (n^0_{p\text{-CNB}} - n_{p\text{-CNB}})/((\text{load of Pt} \times m\ (\text{cat.}) \times (\text{Pt dispersion})/195.084) \times \text{reaction time})$$

2.4 Catalyst characterization

X-ray diffraction (XRD) of samples was performed on a Rigaku D/max-II/2500 X-ray powder diffractometer with Cu Kα radiation and the working voltage and current were 40 kV and 30 mA, respectively. Scanning electron microscopy (SEM) images were collected on a ZEISS Sigma 300 to observe the morphology. Transmission electron microscope (TEM) images were obtained with a JEOL JEM-2100F at an acceleration voltage of 200 kV. Pt dispersions were measured by pulse adsorption of CO on an AutoChem II 2920 automated characterization system at 50 °C. The samples were pretreated in a 5 vol% H_2/95 vol% Ar flow at 673 K for 2 h. The degree of dispersion and the mean particle size were estimated from the measured CO uptake, assuming a cross-sectional area for a surface platinum atom of 8.0×10^{-20} m^2 and a stoichiometric factor of one, using the nominal

platinum concentrations. The H_2 temperature-programmed reduction (TPR) technique was performed using a Microtrac BELCat II, with the samples pretreated in a He flow at 400 °C for 1 h, cooled to 50 °C, and then heated from 50 to 800 °C at 10 °C min^{-1} in a 10% H_2–Ar flow. The content of Pt in the catalysts was measured on an ICP-AES 7300DV instrument. X-ray photoelectron spectroscopy (XPS) was performed using an ESCALAB 250Xi (Thermo) with Al Kα radiation. The specific surface areas of the samples were calculated by the BET method by N_2 adsorption–desorption using a NOVA-2200e volumetric adsorption analyzer.

3 Results and discussion

3.1 Characterization

The crystal phase information of Pt and ZrO_2 in catalysts was obtained by XRD and the patterns are depicted in Fig. 1. The ZSM-5, ZrO_2/ZSM-5, and Pt/ZZ samples exhibit typical diffraction peaks corresponding to ZSM-5 (Fig. 1a). MCM-22, ZrO_2/MCM-22, and Pt/ZM all exhibit typical diffraction peaks, corresponding to MCM-22 (Fig. 1b). Both ZrO_2 and ZrO_2/ZSM-5 (ZrO_2/MCM-22) were prepared by the same method, and ZrO_2 exhibited diffraction peaks of monoclinic and tetragonal ZrO_2. But the characteristic ZrO_2 peaks of the Pt/ZZ and Pt/ZM catalysts with 10% loading in the XRD patterns were not detected.

Generally, the reasons why the component cannot be detected by XRD were as follows: (1) the content is too low; (2) it is in an amorphous glassy state; (3) it interacts to form a solid melt. In our previous work,[34,35] ZrO_2/AC with the same ZrO_2 content was prepared using the same method. The XRD patterns of the ZrO_2/AC samples showed distinct present ZrO_2 peaks, indicating that ZrO_2 was mainly coated on the surface of the AC (1419 $m^2 g^{-1}$). In this work, since ZSM-5 (442 $m^2 g^{-1}$) and MCM-22 (602 $m^2 g^{-1}$) have large specific surface areas, the lack of distinct ZrO_2 diffraction peaks in their XRD patterns can be attributed to monolayer dispersion of ZrO_2 within the channels of ZSM-5 or MCM-22, which inhibits crystal growth. Notably, no diffraction peaks of Pt were detected in related samples due to the relatively low loading (~0.08%), small particle size, and high metal dispersion.

Furthermore, the physical structure of the catalysts was analyzed using N_2 adsorption–desorption. The calculated BET specific surface areas of the samples are listed in Table 1, and the specific surface areas of Pt/ZZ (195 $m^2 g^{-1}$) and Pt/ZM (380 $m^2 g^{-1}$) were lower than those of ZSM-5 (442 $m^2 g^{-1}$) and MCM-22 (602 $m^2 g^{-1}$). Meanwhile, the pore volume of zeolite slightly decreased after the introduction of Pt and ZrO_2, indicating that

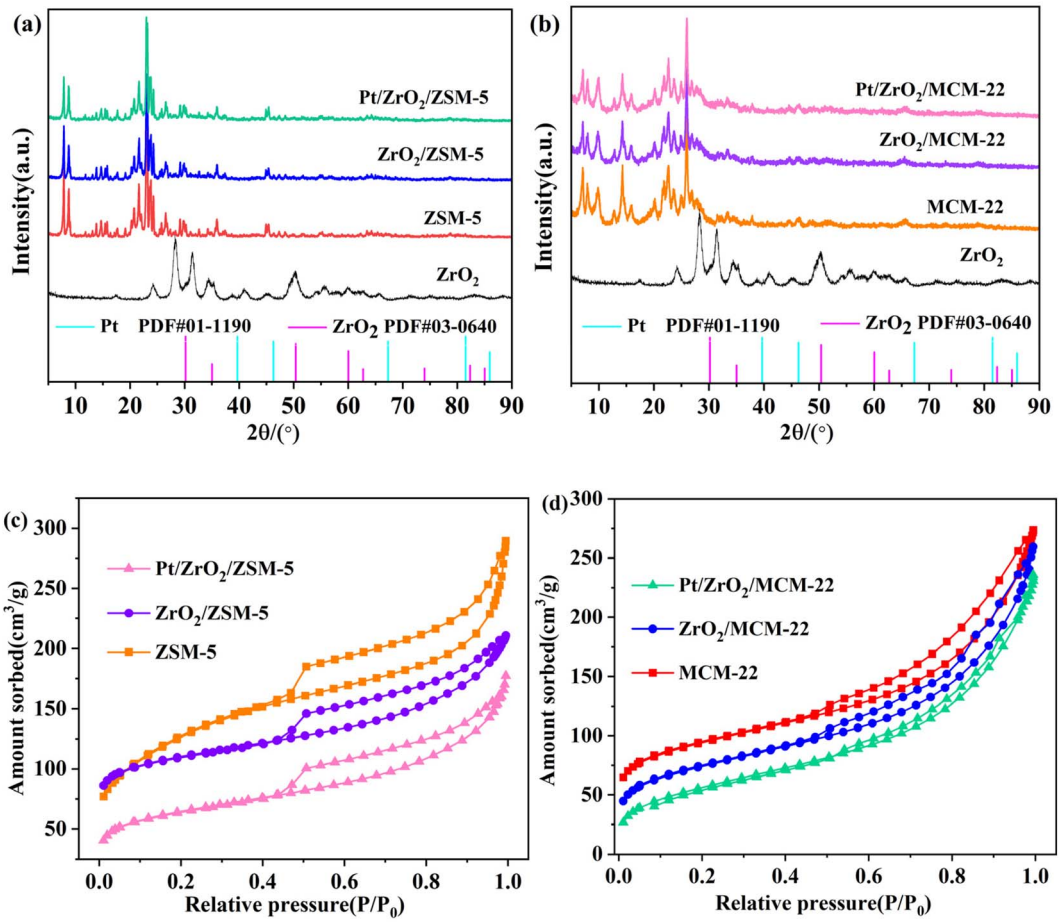

Fig. 1 XRD patterns (a and b) and N_2 adsorption–desorption isotherms (c and d) of Pt catalysts.

Table 1 The physico-chemical characteristics of the samples

Sample	Surface area[a] ($m^2\ g^{-1}$)	Pore volume[a] ($cm^3\ g^{-1}$)	Pt loading[b] (wt%)	Pt size[c] (nm)	Pt dispersion[c] (%)
ZSM-5	442	0.422	—	—	—
ZrO_2/ZSM-5	364	0.319	—	—	—
Pt/ZZ	195	0.131	0.087	1.55	63.1
MCM-22	602	1.121	—	—	—
ZrO_2/MCM-22	429	0.436	—	—	—
Pt/ZM	380	0.411	0.082	2.25	43.5

[a] Determined by N_2 adsorption. [b] Determined by ICP. [c] Determined by CO chemisorption.

Pt nanoparticles and ZrO_2 occupied some of the pores and surface, resulting in a decrease in the specific surface area and pore volume after loading of Pt species. Combined with the N_2 adsorption–desorption isotherms (Fig. 1c and d), all ZSM-5 based samples exhibited a typical IV-type isotherm, indicating their microporous structure.[35] Additionally, the isotherm curves of all MCM-22 based samples exhibit a Type IV pattern with an H4 hysteresis loop, suggesting the presence of mesoporous structures.[36] These results indicate that Pt/ZZ and Pt/ZM successfully maintain the zeolite structure, making them suitable catalysts for the hydrogenation of *p*-CNB.

A scanning electron microscope (SEM) and transmission electron microscope (TEM) were used to investigate the morphology and porous structure of the samples (Fig. 2). As can be seen from Fig. 2a–d, Pt/ZZ displayed a well-defined hexagonal or cuboid crystal morphology with some small particles on

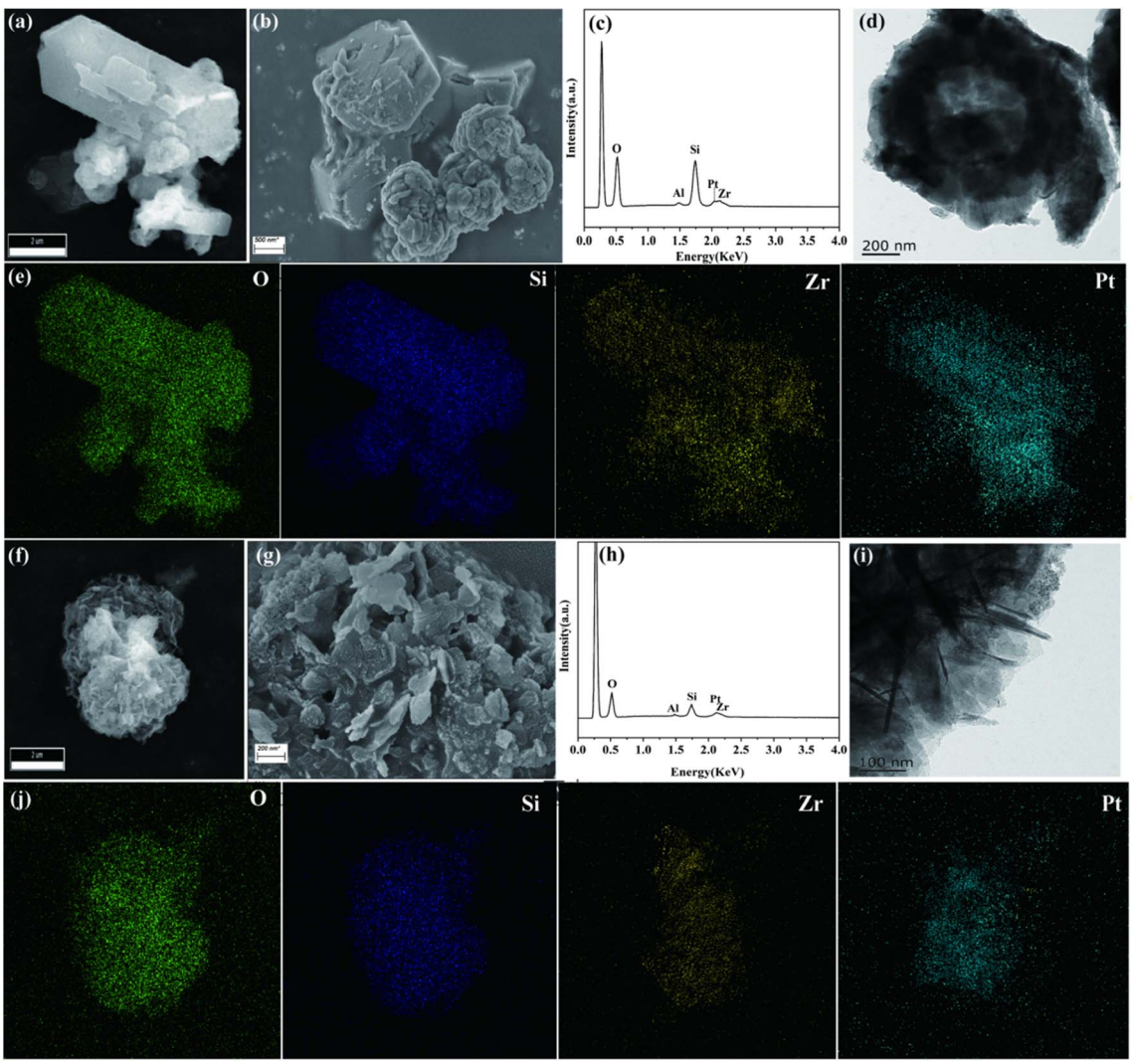

Fig. 2 SEM, TEM images and EDS mapping of Pt/ZZ (a–e) and Pt/ZM (f–j).

the outer surface, resulting in a rough surface. The EDS mapping showed that Pt/ZZ displayed uniform and high dispersion of Pt nanoparticles and ZrO_2. CO chemisorption determined the distribution of Pt on the surface based on the amount of CO adsorbed and calculated the particle size of Pt nanoparticles, and the Pt dispersion and size were 63.1% and 1.55 nm, respectively (Table 1). For Pt/ZM (Fig. 2f–i), the morphology consisted of layered particles formed by a thin interpenetrating network. Similarly, uniform dispersion of Pt nanoparticles and ZrO_2 was confirmed by EDS mapping (Fig. 2j). Accordingly, the CO chemisorption showed that the Pt dispersion and size of Pt/ZM were 43.5% and 2.25 nm, respectively.

X-ray photoelectron spectroscopy (XPS) was further performed to investigate the electronic properties. The high-resolution spectra of Zr 3d peaks are shown in Fig. 3a. For Pt/ZrO_2, two valence states of Zr are observed at the binding energies of around 182.1 and 184.6 eV for $Zr^{3+}(3d_{5/2})$ and $Zr^{3+}(3d_{3/2})$, and 182.7 and 185.1 eV for $Zr^{4+}(3d_{5/2})$ and $Zr^{4+}(3d_{3/2})$, respectively. The binding energies of Zr^{3+} $3d_{5/2}/3d_{3/2}$ and Zr^{4+} $3d_{5/2}/3d_{3/2}$ for Pt/ZZ are about 181.9/184.4 and 182.6/185.0 eV, respectively. The Zr^{3+} $3d_{5/2}/3d_{3/2}$ and Zr^{4+} $3d_{5/2}/3d_{3/2}$ peaks of Pt/ZM are centered at 182.4/184.7 and 183.2/185.6 eV, respectively. The presence of Zr^{3+} peaks can be attributed to the unsaturated coordination of Zr sites with defective O atoms in ZrO_2,[37] demonstrating a strong metal–support interaction between Pt nanoparticles and ZrO_2 that facilitates electron transfer. The Pt 4f XPS spectrum (Fig. 3b) of Pt/ZrO_2 shows four peaks at the binding energies of 75.6, 72.2, 76.6, and 73.4 eV. The first two binding energies can be assigned to the $4f_{5/2}$ and $4f_{7/2}$ peaks of Pt^0 species, while the last two can be assigned to the $4f_{5/2}$ and $4f_{7/2}$ peaks of $Pt^{\delta+}$ species. For the Pt/ZZ catalyst, the binding energies at 75.0/71.6 and 76.3/72.9 eV can be assigned to the $4f_{5/2}/4f_{7/2}$ of Pt^0 and $Pt^{\delta+}$ species, respectively. For Pt/ZM, the Pt $4f_{5/2}$ and Pt $4f_{7/2}$ peaks were at 75.4/72.0 and 76.5/73.1 eV, respectively. Compared with Pt/ZrO_2, the binding energy of Pt species in Pt/ZZ and Pt/ZM showed negative shifts, indicating partial electron transfer from Pt to ZrO_2. In addition, according to the XPS results (Table S1†), the percentages of $Pt^0/Pt^{\delta+}$ of Pt/ZrO_2, Pt/ZZ, and Pt/ZM are calculated to be 48.9/51.1, 57.1/42.9, and 52.8/47.2, respectively, reflecting a significant electron transfer between Pt species and ZrO_2. Specifically, the binding energy of Pt decreases more in Pt/ZM, further confirming the stronger interaction between Pt and ZrO_2 in this sample. However, due to the overlap of the core energy levels of the Pt 4f and Al 2p spectra, analysis of the interaction based on the binding energy of Pt species is insufficient. Therefore, the Pt 4d spectrum of Pt/ZZ and Pt/ZM was recorded, and the corresponding results are shown in Fig. 3c. For Pt/ZZ, the Pt $4d_{5/2}$/Pt $4d_{3/2}$ regions located at 314.1/331.8 and 315.5/333.1 eV were attributed to Pt^0 and

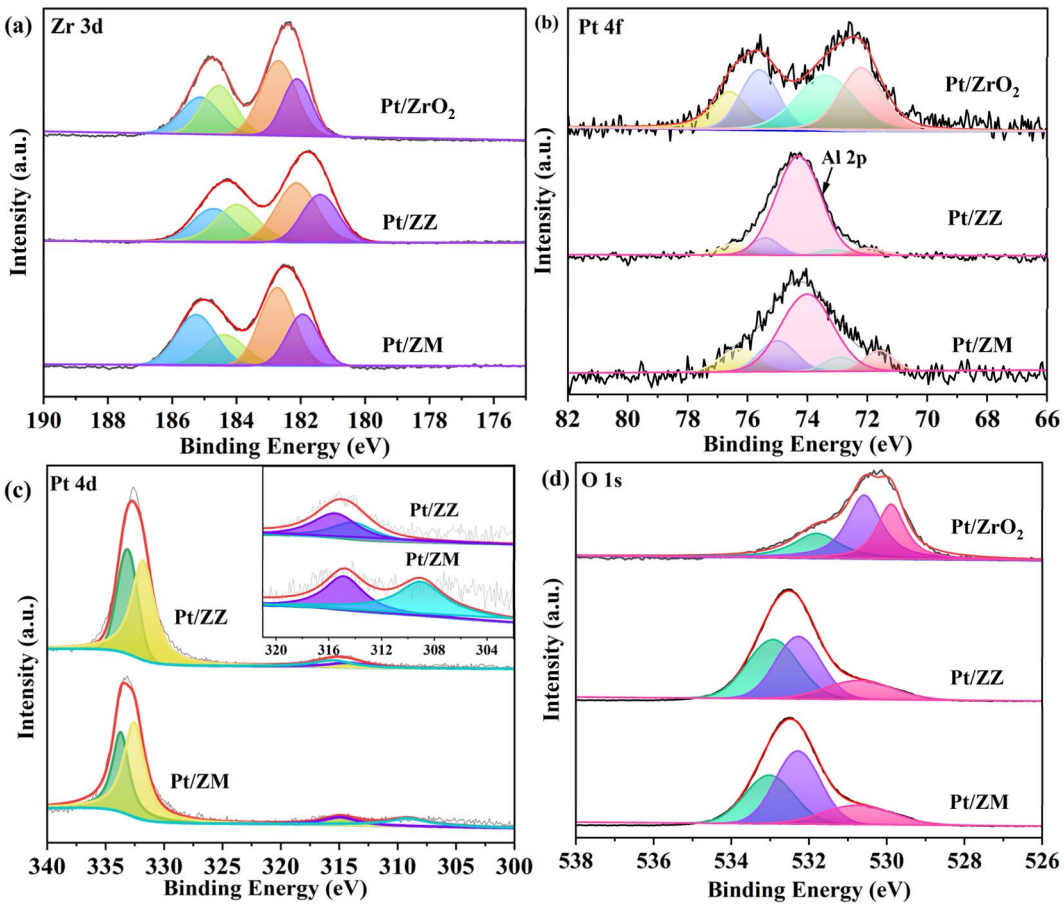

Fig. 3 Zr 3d (a), Pt 4f (b), Pt 4d (c), and O 1s (d) XPS spectra of the samples.

Pt^{2+}, respectively. The Pt 4d core level spectra of Pt/ZM were also deconvoluted into four peaks that were attributed to Pt^0 and Pt^{2+}.[38,39] In addition, the Pt 4d peaks of Pt/ZZ and Pt/ZM were both shifted to higher binding energies compared with the typical Pt $4d_{5/2}$ (314.5 eV) and Pt $4d_{3/2}$ (331.2 eV), indicating that the electrons were transferred from Pt to ZrO_2, and the percentages of $Pt^0/Pt^{\delta+}$ of Pt/ZZ and Pt/ZM were calculated to be 60.5/39.5 and 57.9/42.1, respectively.

Because of the presence of Zr^{3+}, oxygen vacancies form to achieve the charge balance. In the O XPS spectra shown in Fig. 3d, O_α, O_β and O_γ represent the O element in the lattice, oxygen vacancy,[40] and adsorbed oxygen, respectively.[41] By calculating the proportion of the O species (Table S2†), the O_β of Pt/ZrO_2, Pt/ZZ, and Pt/ZM was 44.8, 39.8, and 47.2%, respectively. This result indicates that more oxygen vacancies were generated in Pt/ZM, which can be attributed to the electron transfer from Pt to ZrO_2. Clearly, the characterization data validate the significant structural and electronic properties in these catalysts, which should significantly influence the catalytic reactivity.

The H_2 consumption peaks at low and high reduction temperatures were assigned to the reduction of PtO with weak and strong interactions with the support.[38,41,42] Fig. 4 shows the H_2-TPR profiles of Pt catalysts. All samples showed two main signals centered at 70–90 °C and 550–650 °C. The first signal can be ascribed to the reduction of PtO_x species, while the second can be assigned to the reduction of PtO_x species having a stronger interaction with the support. For Pt/ZrO_2, the reduction requires a slightly higher temperature (82.5 °C and 616 °C), indicating a relatively strong metal–support interaction. In addition, a negative peak at about 560 °C was detected, assigned to the bulk oxygen in ZrO_2.[43] Pt/ZZ exhibited two reduction peaks centered at 73.7 °C and 569.7 °C, and these peaks are slightly shifted to lower temperature compared to the corresponding peak of the Pt/ZrO_2, suggesting that the support (ZSM-5 and MCM-22) influences the reduction of PtO_x. In Pt/ZM, two peaks in the temperature range of 80–200 °C were clearly observed, one main peak (73.7 °C) assigned to PtO_x and the other main peak at 173.2 °C related to the reduction of Pt^{2+} cations. The reduction region of strong interaction is restricted to a broader band centered around 400–600 °C, and the possible reason was the electron transfer and a strong interaction between Pt and ZrO_2/MCM-22. All the results discussed so far suggest that a specific interaction exists between Pt and the support, and these metal–support interactions are strongly support dependent.

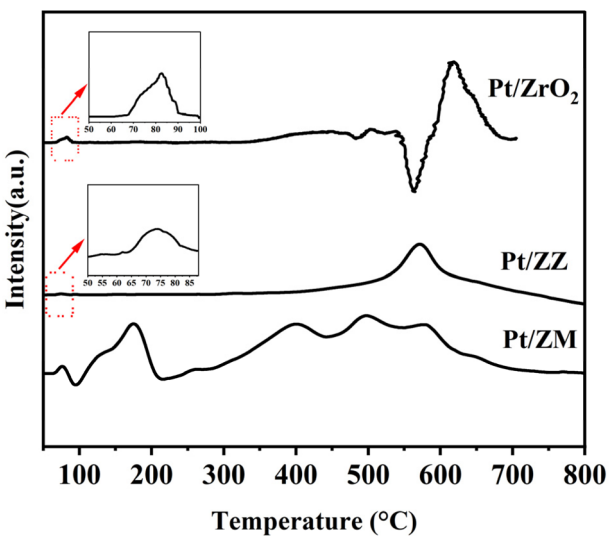

Fig. 4 H_2-TPR profiles of Pt catalysts.

3.2 Hydrogenation of *p*-CNB

In this study, hydrogenation of *p*-CNB to aniline was chosen as a model reaction to demonstrate the catalytic advantage of Pt/ZZ and Pt/ZM (Fig. 5). For comparison, we also examined the performance of traditional Pt/ZrO_2, Pt/ZSM-5, and Pt/MCM-22. Firstly, as shown in Fig. 5a, Pt/ZSM-5 and Pt/MCM-22 showed very poor activity under identical conditions, and 36.1% and 3.8% conversions for *p*-CAN were observed, respectively. In contrast, both Pt/ZZ and Pt/ZM exhibited exceptional catalytic activity, showing both outstanding conversion (>98%) and selectivity (>99.9%) and almost undetectable by-product aniline (AN). As can be seen, for the hydrogenation of *p*-CNB over the Pt/ZZ catalyst, the conversion of *p*-CNB was 2.76-fold higher than that of Pt/ZSM-5, and the Pt/ZM catalyst showed 25.8-fold higher conversion than Pt/MCM-22, indicating that the suitable amount of ZrO_2 at the Pt/zeolite interface favors adjustment of the structure. Thus, the difference in conversion should be ascribed to the electronic modification of Pt from complex supports. These results clearly demonstrate the advantages of this particular unconventional structural catalyst in this hydrogenation system. Obviously, the Pt/ZZ and Pt/ZM catalysts exhibited a synergistic effect, which can greatly enhance the performance of *p*-CNB hydrogenation by modulating the electronic structure and surface structure.

In addition, Pt/ZrO_2 afforded 17.0% conversion of *p*-CNB and 100% selectivity, and the catalytic activity was also lower than that of Pt/ZZ and Pt/ZM. On the one hand, the small specific surface area (52 $m^2\ g^{-1}$), low Pt dispersion (8.5%), and relatively larger Pt size (5.65 nm) are not conducive to the hydrogenation reaction. On the other hand, although there is also an electronic effect caused by the electron transfer between Pt and ZrO_2 in Pt/ZrO_2, the negative impact of the size effect outweighs the positive influence of the electronic effect, resulting in unsatisfactory activity.

Then, the hydrogenation of *p*-CNB was performed using the Pt/ZZ and Pt/ZM catalysts at 40 °C, as shown in Fig. 5b. The *p*-CNB conversion increased from <20% at 20 min to >99.9% at 90 min, while the selectivity of *p*-CAN stayed at 99.9%. Significantly, although the Pt content was only 0.08%, the Pt/ZZ and Pt/ZM catalysts achieved >99% conversion, indicating that the strong synergistic effect within them fully developed the catalytic ability of Pt, thus reducing the Pt usage.

It seems that Pt/ZZ and Pt/ZM have similar catalytic activity. In Fig. 5c and Table S3,† the relative parameters and figures regarding the *p*-CNB conversion rate with reaction time show

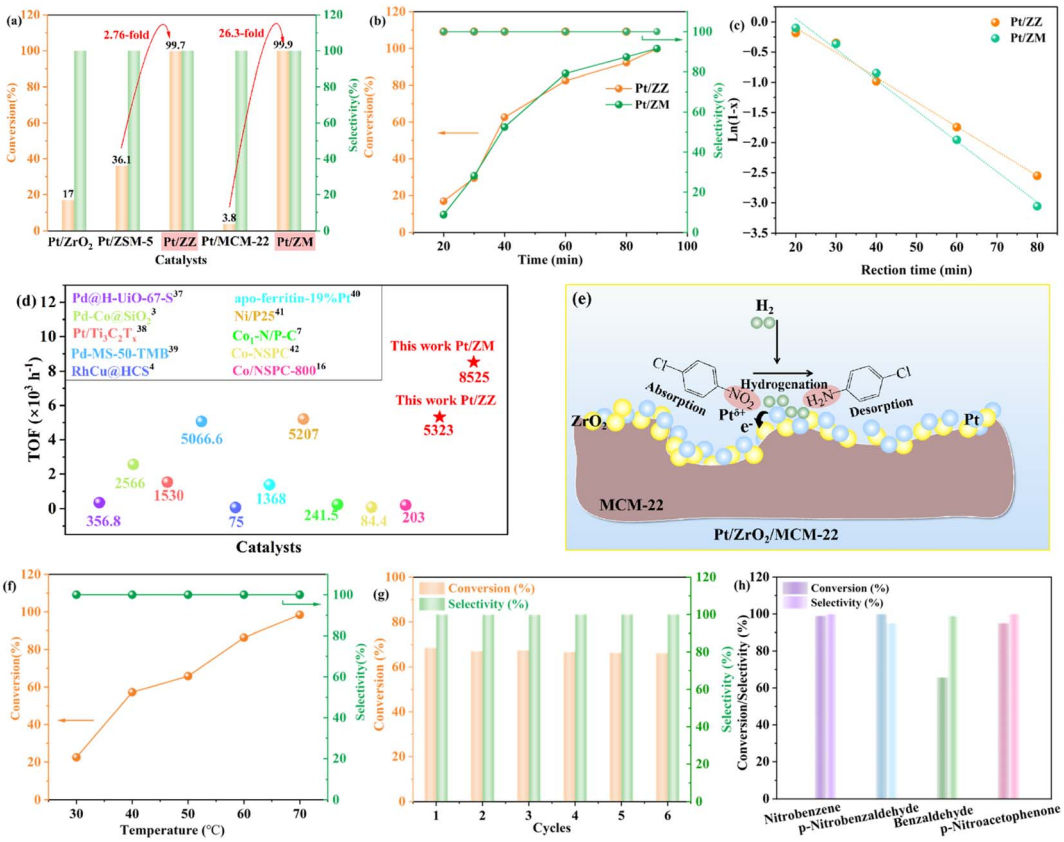

Fig. 5 Catalytic performance of the catalysts in hydrogenation of *p*-CNB (a); effects of reaction time on *p*-CNB conversion and selectivity over Pt/ZZ and Pt/ZM (b); kinetic profiles (X represents the conversion) for the hydrogenation of *p*-CNB over Pt/ZZ and Pt/ZM (c); comparison of the TOF with reported catalysts[3,4,7,16,45–50] (d); schematic diagram of *p*-CNB hydrogenation over the Pt/ZM catalyst (e); influence of temperature on the catalytic performance of Pt/ZM (f); stability test of the Pt/ZM catalyst (g); activity of Pt/ZM catalysts for hydrogenation of other substrates (h). Reaction conditions: [a]Cat. (0.1 g), [b]*p*-CNB (0.4 g), [c]ethanol (20 mL), [d]40 °C, [e]H_2 (0.7 MPa), 90 min; [f]40 min; [g]50 min.

that both samples fit a pseudo-first-order kinetic model. However, the reaction rate of the Pt/ZM catalyst (1.068 min^{-1}) is higher than that of Pt/ZZ (0.718 min^{-1}). Moreover, the TOF of Pt/ZM is as high as 8525 h^{-1}, much higher than that of Pt/ZZ (5323 h^{-1}) (Fig. 5d). Generally, the smaller the nanoparticle size and the higher the dispersion, the higher the catalytic activity. Despite Pt/ZZ having a more favorable Pt size (1.55 nm) and dispersion (63.1%), its catalytic activity was behind that of Pt/ZM. This result indicates that the size effect is not dominant in this hybrid nano-structured catalyst, and the most possible reason may be the electronic effect. Indeed, the potential to enhance catalytic activity by modulating the electronic structure has been observed previously.[12,44] Due to electron transfer from Pt to ZrO_2 nanoparticles, the $Pt^{\delta+}$ percentage of Pt/ZM (42.1%) is higher than that of Pt/ZZ (39.5%). The electron-deficient Pt site is more favorable for *p*-CNB adsorption, and as the fraction of $Pt^{\delta+}$ increases, the catalytic activity increases.

Next, the effect of the Pt loading amount on the catalytic performance was investigated (Table S4†). The activity gradually increased with the increase of the Pt loading amount from 0.087% to 2.7%, and all these catalysts exhibited >99% conversion but required much shorter reaction times.

Finally, Pt/ZZ and Pt/ZM were also compared with the latest reported catalysts, and the results are displayed in Fig. 5d and Table S5.† Remarkably, the catalytic performance of Pt/ZZ and Pt/ZM surpasses that of most reported noble metal and novel non-noble metal catalysts. Notably, although these nano-structured Pt/ZZ and Pt/ZM have low Pt loading, they exhibited superior catalytic activity under mild reaction conditions, demonstrating that the developed strategy of supporting Pt on complex supports is effective in promoting the activity of supported Pt catalysts.

To gain deep insight into the hydrogenation process of the Pt/ZM catalyst, experiments were conducted at different temperatures under the same conditions (Fig. 5f). The conversion of *p*-CNB significantly increased from 22.5% to 98.4% as the reaction temperature was increased from 30 to 70 °C, while the selectivity to *p*-CAN was maintained at >99.9%, with almost no intermediate or by-product observed, indicating that Pt nanoparticles diffused in the pores of the support could effectively adsorb *p*-CNB and desorb *p*-CAN appropriately. As the temperature increases, the rapid consumption of *p*-CNB indicates that the hydrogenation of *p*-CNB to *p*-CAN is more favorable at elevated reaction temperature.

Then, the reusability of the Pt/ZM catalyst is shown in Fig. 5g. The catalyst was recycled through filtration, washing, and drying, and the conversions were 68.6, 67.1, 67.5, 66.8, 66.5, and 66.2% for the first to the sixth run, respectively. Moreover, the selectivity for *p*-CAN remained unchanged. The TEM image (Fig. S1†) of the Pt/ZM catalyst after several tests showed negligible differences compared with the fresh sample, implying the good retention of its structure. The unique structure of MCM-22 provided a limited spatial volume to anchor Pt nanoparticles and ZrO_2, which contributed to the Pt/ZM catalyst maintaining its structure and activity. In conclusion, the Pt/ZM catalyst was efficient and reusable.

Subsequently, other substrates were also employed to investigate the properties of the Pt/ZM catalyst, and the results are shown in Fig. 5h. There is no doubt that the Pt/ZM catalyst shows good catalytic performance for nitrobenzene, affording the corresponding aniline with excellent conversion (>99%). In addition, *p*-nitrobenzaldehyde, an industrially important drug and pesticide intermediate, can be easily obtained by completely hydrogenating the corresponding nitroarene within 60 min with a 100% conversion. For the hydrogenation of benzaldehyde, the conversion can reach more than 65% with more than 98% selectivity. These results strongly indicate that the Pt/ZM catalyst preferentially adsorbs the nitro group and is a highly selective and effective catalyst for hydrogenating nitroarenes. In the case of *p*-nitroacetophenone, the conversion decreased slightly (95%), which may be due to the steric effect of the substituent group on the catalytic hydrogenation rates.

On the basis of the above results and previous literature reports,[8,12,46] we propose a plausible catalytic mechanism for the hydrogenation of *p*-CNB over the Pt/ZM catalyst, as shown in Fig. 5e. The micropores of MCM-22 provide a limited spatial volume to anchor Pt nanoparticles and ZrO_2, and the appropriate content of ZrO_2 ensures the electron effect between Pt nanoparticles and ZrO_2, forming the unique structure of Pt/ZM. On the one hand, the high specific surface area provides a perfect place for hydrogenation. On the other hand, MCM-22 micropores changed the spatial disposition of the adsorption of *p*-CNB on Pt sites in contact with these micropores, and the electron effect promoted the hydrogenation process. Hence, when *p*-CNB is adsorbed on Pt/ZM, it preferentially adsorbs onto $Pt^{\delta+}$ sites *via* the nitro group rather than the chloro group due to the strong interaction of the nitro group with the Pt surface, while H_2 molecules were dissociated and activated on the Pt^0 sites. Then, the nitro groups adsorbed on the catalyst undergo hydrogenation with hydrogen ions to form *p*-CAN. Simultaneously, the hydrogenolysis of the carbon–chlorine bond is suppressed, reducing byproduct formation and ensuring high selectivity for *p*-CAN.

4 Conclusion

In conclusion, we developed Pt catalysts with low loading but high performance by combining ZrO_2 and zeolite as a complex support. The obtained Pt/ZZ and Pt/ZM catalysts exhibited a synergistic effect and demonstrated outstanding activity and excellent selectivity for selective hydrogenation of *p*-CNB to *p*-CAN, achieving TOFs of 5323 h^{-1} and 8525 h^{-1}, respectively. Notably, the optimal Pt/ZM exhibited the best catalytic activity and good recyclability. Catalyst characterization indicated that the electron transfer from Pt to ZrO_2 increased the fraction of electron-deficient Pt, which is more favorable for *p*-CNB adsorption, thereby enhancing catalytic activity. We believe that combining noble metals with metal oxides/zeolites to design high-efficiency, low-noble-metal-loading catalysts opens a new avenue for noble metal catalysts. This research also provides new ideas and insights for optimizing heterogeneous catalysts for chemoselective hydrogenation.

Data availability

The data supporting this article have been included as part of the ESI.†

Conflicts of interest

The authors declare no conflict of interest.

Acknowledgements

This work was supported by the Natural Science Foundation of Zhejiang Province (LQ24B060005) and the Quzhou University PhD Research Start-up Project (BSYJ202103).

References

1 L. Gao, J. Liu, X. Zhong, Y. Zhang, J. Chen, M. Shakeri, X. Zhang and B. Zhang, *ACS Appl. Nano Mater.*, 2023, 5685–5691.
2 A. Afzalinia and M. Mirzaee, *J. Mol. Struct.*, 2023, 135322.
3 L. Xiao, C. Chuanqi, L. Zhixi, Z. Chaoyang, D. Jing, S. Meina, W. Yue, L. Shaopeng, G. Jun and M. Zhao, *Nano Res.*, 2023, **16**, 11334–11341.
4 F. Yang, H. Yu, C. Wu, S. Wang, T. Li and H. Yin, *ACS Appl. Nano Mater.*, 2022, 11627–11635.
5 D. Liu, N. Ismail, F. Chaohe, H. Kuan, G. Binghui, C. Hailong and C. Zhuo, *Appl. Catal., A*, 2022, 118840.
6 L. Geng, F. Geng, X. Cheng, X. Wang, L. Wang, X. Pang, Y. Zhang, X. Zhang, D. Zhang, S. Zhuang, A. Abdukayum and G. Hu, *Appl. Surf. Sci.*, 2024, **657**, 159775.
7 F. Cao, W. Ni, Q. Zhao, L. Wang, S. Xue, Y. Li, D. Kong, M. Wu and L. Zhi, *Appl. Catal., B*, 2024, 123762.
8 G. Yue, Y. Yu, S. Li, H. Li, S. Gao, Y. Wang, W. Guo, N. Wang, X. Li, Z. Cui, C. Cao, L. Jiang and Y. Zhao, *Small*, 2023, 2207918.
9 K. P. Reddy, C. Swetha and A. Murugadoss, *ACS Sustainable Chem. Eng.*, 2023, 1643–1654.
10 F. Zhang, Y. Jiang, S. Dai, X. Wei, Y. Ma, H. Liao, Y. Qin, Q. Peng, X. Zhao and Z. Hou, *Ind. Eng. Chem. Res.*, 2023, **62**, 5814–5825.
11 X. Zhang, Z. Li, W. Pei, G. Li, W. Liu, P. Du, Z. Wang, Z. Qin, H. Qi, X. Liu, S. Zhou, J. Zhao, B. Yang and W. Shen, *ACS Catal.*, 2022, **12**, 3634–3643.

12 Z. Wang, C. Wang, S. Mao, B. Lu, Y. Chen, X. Zhang, Z. Chen and Y. Wang, *Nat. Commun.*, 2022, **13**, 3561.
13 M. Cheng, P. Lv, X. Zhang, R. Xiong, Z. Guo, Z. Wang, Z. Zhou and M. Zhang, *J. Catal.*, 2021, **399**, 182–191.
14 N. Zengin, H. Goksu and F. Sen, *Chemosphere*, 2021, 130887.
15 B. Lu, X. Chen, C. Feng, J. Chang and F. Ye, *ACS Appl. Nano Mater.*, 2021, **4**, 2278–2284.
16 J. Xu, X. Chen, J. Bai, Z. Miao, Y. Tan, N. Zhan, H. Liu, M. Ma, M. Cai, Q. Cheng and S. Sun, *Catal. Sci. Technol.*, 2024, **14**, 1167–1180.
17 B. Han, Y. Guo, Y. Huang, W. Xi, J. Xu, J. Luo, H. Qi, Y. Ren, X. Liu, B. Qiao and T. Zhang, *Angew. Chem., Int. Ed.*, 2020, **59**, 11824–11829.
18 G. Chen, J. Han, Z. Niu, P. She, L. Li, B. Guan and J. Yu, *J. Am. Chem. Soc.*, 2023, **145**, 9021–9028.
19 G. Tian, G. Chen, G. Yang, Z. Diao, R. Bai, J. Han, B. Guan and J. Yu, *ACS Cent. Sci.*, 2024, **10**, 1473–1480.
20 G. Yang, Y. He, C. Zhang, Z. Sun, M. Han, P. Peng, Y. Yue, H. Liu, L. Liu, J. Chen, L. Bai and Q. Chen, *ChemCatChem*, 2023, **15**, e202300969.
21 T. Li, S. Wang, H. Yu, L. Yuan, D. Zhang and H. Yin, *Ind. Eng. Chem. Res.*, 2022, 18762–18771.
22 Y. T. Wang, S. M. Wu, G. Q. Luo, S. T. Xiao, F. F. Pu, L. Y. Wang, G. G. Chang, G. Tian and X. Y. Yang, *Chem.–Asian J.*, 2023, **18**, e202300689.
23 J. Ma, X. Mao, C. Hu, X. Wang, W. Gong, D. Liu, R. Long, A. Du, H. Zhao and Y. Xiong, *J. Am. Chem. Soc.*, 2024, **146**, 970–978.
24 Q. Zhang, J. Bu, J. Wang, C. Sun, D. Zhao, G. Sheng, X. Xie, M. Sun and L. Yu, *ACS Catal.*, 2020, 10350–10363.
25 D. Zhu, L. Long, J. Sun, H. Wan and S. Zheng, *Appl. Surf. Sci.*, 2020, **504**, 144329.
26 A. Corma and P. Serna, *Science*, 2006, **313**, 332–334.
27 M. Boronat, P. Concepción, A. Corma, S. González, F. Illas and P. Serna, *J. Am. Chem. Soc.*, 2007, **129**, 16230–16237.
28 A. Corma, P. Serna, P. Concepción and J. J. Calvino, *J. Am. Chem. Soc.*, 2008, **130**, 8748–8753.
29 Y. Zhang, J. Zhou, F. Wang, M. Lv and K. Li, *J. Catal.*, 2023, 12–19.
30 Y. Zhang, J. Zhou, F. Wang and X. Zhao, *Langmuir*, 2022, **38**, 7699–7708.
31 Y. Zhang and J. Zhou, *J. Catal.*, 2021, **395**, 445–456.
32 Y. Zhang and J. Zhou, *Nanotechnology*, 2020, **31**, 295703.
33 Y. Zhang, J. Zhou, K. Li and M. Lv, *Catal. Today*, 2020, **358**, 129–137.
34 Y. Zhang, J. Zhou, K. Li and M. Lv, *Mol. Catal.*, 2019, **478**, 110567.
35 T. Fu, Y. Wang and Z. Li, *Langmuir*, 2020, **36**, 3737–3749.
36 D. Pithadia, A. Patel and V. Hatiya, *Renewable Energy*, 2022, **187**, 933–943.
37 Z. Qin, L. Chen, Y. Li and K. Shen, *ACS Catal.*, 2023, 8372–8383.
38 H. Pan, J. Li, J. Lu, G. Wang, W. Xie, P. Wu and X. Li, *J. Catal.*, 2017, **354**, 24–36.
39 W. Tan, S. Xie, X. Zhang, K. Ye, M. Almousawi, D. Kim, H. Yu, Y. Cai, H. Xi, L. Ma, S. N. Ehrlich, F. Gao, L. Dong and F. Liu, *ACS Appl. Mater. Interfaces*, 2024, **16**, 454–466.
40 J. Wang, Y. Zhang, X. Xu and M. Bao, *ACS Appl. Mater. Interfaces*, 2023, 8149–8156.
41 Q. Wang, G. Wang, H. Xin, J. Liu, G. Xiong, P. Wu and X. Li, *Catal. Sci. Technol.*, 2019, **9**, 3226–3237.
42 J. Lee, E. J. Jang, D. G. Oh, J. Szanyi and J. H. Kwak, *J. Catal.*, 2020, **385**, 204–212.
43 Z. Tang, P. Liu, H. Cao, S. Bals, H. J. Heeres and P. P. Pescarmona, *ACS Catal.*, 2019, **9**, 9953–9963.
44 Y. Zhang, K. Fulajtarova, M. Kubu, M. Mazur, M. Hronec and J. Cejka, *Catal. Today*, 2020, **345**, 39–47.
45 T. M. Bustamante, C. H. Campos, M. A. Fraga, J. L. G. Fierro and G. Pecchi, *J. Catal.*, 2020, **385**, 224–237.
46 X. Li, W. Gao, L. Li, B. Li, M. Chen, Y. Ge, S. Liu, L. Wang, L. Ma, L. Niu, Y. Li, Z. Liu and J. Chen, *ACS Appl. Nano Mater.*, 2024, 14540–14548.
47 W. Yu, H. Lin and C. Tan, *Chem. Eng. J.*, 2017, **325**, 124–133.
48 Y. Zhou, Y. Zheng, C. Lu, B. Maity, Y. Chen, T. Ueno, Z. Liu and D. Lu, *ACS Appl. Nano Mater.*, 2023, 5835–5843.
49 J. Bai, J. Xu, M. Ma, Z. Miao, J. Yu, H. Liu, Z. Qian, M. Cai, Q. Cheng, Y. Jiang and S. Sun, *Langmuir*, 2024, 12179–12190.
50 J. Xu, J. Bai, W. Si, Y. Zhang, J. Tan, M. Cai, Q. Cheng and S. Sun, *Ind. Eng. Chem. Res.*, 2023, 3862–3872.